A Variable Forward-Sweep Wing Design for Improved Perching in Micro Aerial Vehicles

Zachary R. Manchester[*]

Harvard University, Cambridge, Massachusetts, 02138

Jeffrey I. Lipton[†]

Massachusetts Institute of Technology, Cambridge, Massachusetts, 02139

Robert J. Wood[‡] and Scott Kuindersma[§]

Harvard University, Cambridge, Massachusetts, 02138

A micro aerial vehicle with a variable forward-sweep wing is proposed with the goal of enhancing performance and controllability during high-angle-of-attack perching maneuvers. Data is presented from a series of wind tunnel experiments to quantify the aerodynamic effects of forward sweep over a range of angles of attack from -25° to +75°. A nonlinear dynamics model is constructed using the wind tunnel data to gain further insight into aircraft flight dynamics and controllability. Simulated perching trajectories optimized with a direct collocation method indicate that the forward-swept wing configuration can achieve qualitatively different lower-cost perching maneuvers than the straight wing configuration.

I.   Introduction

Fixed-wing unmanned aerial vehicles (UAVs) that emulate the perching capabilities of birds would offer the ability to take off and land within very small spaces, travel long distances, and efficiently loiter for long periods of time. Aircraft with this mix of capabilities have several practical applications including search and rescue, disaster response, agricultural inspection, and retrieval and delivery of terrestrial objects. Perching maneuvers are challenging in several respects. First, they involve flight at extremely high angles of attack in which the airflow around the wings is non-laminar and difficult to model. Second, aircraft control surfaces typically have reduced effectiveness at low speed and in post-stall conditions. Lastly, perching often entails flight in close proximity to, and even in contact with, obstacles that could damage an aircraft.

There has been significant recent progress made on perching with conventional fixed-wing aircraft: More, Cory, and Tedrake demonstrated perching with a simple flat-plate glider [1], and Desbiens, Asbeck, and Cutkosky added a system of spikes to an off-the-shelf remote control airplane that allowed it to land and take off from vertical walls [2]. There have also been a number of related studies involving wing-morphing aircraft. Wickenheiser and Garcia developed an aircraft with a wing that rotated along the chord line to help maintain control during perching [3]. Additionally, the ability to regulate pitch with wing sweep has been demonstrated experimentally by several researchers [4–6].

Forward-swept wings have a number of characteristics that make them well suited to agile flight at high angles of attack. All swept wings have the property that their aft-most sections stall first [7]. In the case of conventional back-swept wings, this corresponds to a stall occurring at the wing tips, resulting in a loss of aileron control. In the case of forward-swept wings, however, stall occurs first at the wing root, leaving the ailerons fully effective. This phenomenon was dramatically demonstrated by the Grumman X-29 (Figure 1), which was capable of performing a "wing rock" maneuver well into the post-stall regime at a 67° angle of attack [8].

In addition to maintaining roll control at high angles of attack, forward-swept wings also offer enhanced yaw maneuverability [8]. This, however, comes at the cost of passive stability, and necessitates constant closed-loop feedback stabilization. Such frequent control inputs decrease the aerodynamic efficiency of the aircraft in level flight by causing increased drag and also place an additional burden on the onboard power system and actuators. To take advantage of the benefits of forward sweep during perching and other aggressive maneuvers while maintaining passive stability and efficient gliding during level flight, a variable-sweep wing is necessary. As in many other areas of aviation,

---

[*]Postdoctoral Fellow, Paulson School of Engineering and Applied Sciences, 60 Oxford Street, Member
[†]Postdoctoral Research Associate, Computer Science and Artificial Intelligence Laboratory, 32 Vassar Street
[‡]Professor, Paulson School of Engineering and Applied Sciences, 33 Oxford Street
[§]Assistant Professor, Paulson School of Engineering and Applied Sciences, 33 Oxford Street

Figure 1. Forward-swept wings in aviation and in nature. Left: The Grumman X-29 experimental aircraft flying at a high angle of attack. Right: A brown eagle sweeps its wings forward during a "snatching" maneuver.

birds provide much inspiration for this work. In particular, many species have been observed to sweep their wings forward during high angle of attack perching and "snatching" maneuvers [9] (Figure 1).

In this paper we evaluate the effectiveness of forward-swept wing designs on lightweight UAVs through a series of wind-tunnel and simulation experiments. We begin by describing a prototype lightweight sweeping mechanism (Section II) that can be retrofitted to an off-the-shelf foam micro aerial vehicle (MAV). Sections III and IV then document the experimental methods and results of wind tunnel tests performed with models of the MAV in different wing-sweep configurations. The data collected in these tests shows that the forward-swept wing configuration has a higher peak lift coefficient and lower pitching moment at high angles of attack, both of which are beneficial in perching maneuvers. Section V develops a nonlinear flight dynamics model using the aerodynamic coefficients collected in the wind tunnel. The model is then used in combination with numerical trajectory optimization methods to calculate and simulate perching trajectories (Section VI). Theses numerical experiments show that the forward-swept wing is capable of achieving "more optimal" perching trajectories that require less actuator effort.

II.   Variable-Sweep Wing Design

The starting point for our wing-morphing aircraft was the low-cost flat-foam hobby aircraft shown in Figure 2, which has a wingspan of 42 centimeters and a mass of 37 grams. Several objectives guided the design of the wing sweeping mechanism. First, we sought to make minimal modifications to the original airplane. Second, the mechanism needed to be extremely lightweight to minimize the impact on flight performance. Lastly, we wanted to drive the mechanism with the same small linear servos used to actuate the control surfaces on the airplane.

Figure 3 depicts our single-degree-of-freedom modified sliding-crank mechanism design. The red links are attached to the wings, while the yellow link is fixed to the fuselage. The pivot point locations were chosen to provide a 25° sweep angle and to allow the ailerons to clear the fuselage. Several prototypes have been constructed from laser-cut fiberglass and carbon fiber to provide high stiffness and low weight. A fully assembled airplane with the sweeping mechanism installed is shown in Figure 2. In the remainder of the paper, we analyze the aerodynamic properties of the airplane at the extreme configurations of 0° and 25° and leave flight experiments with the variable-sweep aircraft to future work.

III.   Wind Tunnel Test Setup

To gain insight into the aerodynamics of the forward-swept wing configuration, experiments were conducted at Harvard University's Concord Field Station (CFS) wind tunnel. Measurements of aerodynamic lift, drag, and moment were made over a range of angles of attack from −25° to +75°. In addition, the roll moment generated by an aileron deflection of 20° was measured over the same range of angles of attack to identify differences in high-angle-of-attack control authority.

The CFS wind tunnel has a test section 1.2×1.2 meters in cross section and 1.4 meters in length and is capable of operating at wind speeds from 0 to 28.5 m/s. A schematic diagram is shown in Figure 4. The test section is constructed of transparent Lexan panels, allowing cameras and lighting equipment to be placed outside the tunnel. Details of its design, construction, and calibration can be found in [10].
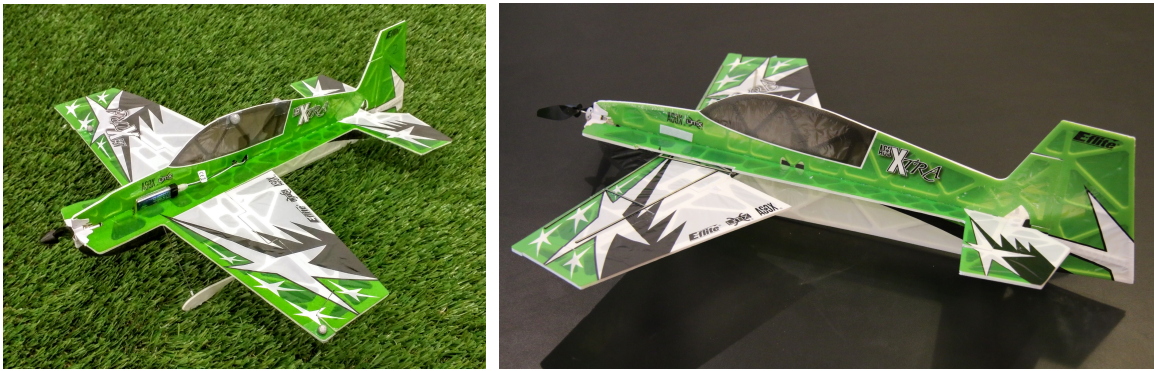
American Institute of Aeronautics and Astronautics

Figure 2. Unmodified E-Flite AS3Xtra aircraft (left) and modified aircraft showing wing in forward-swept configuration (right).
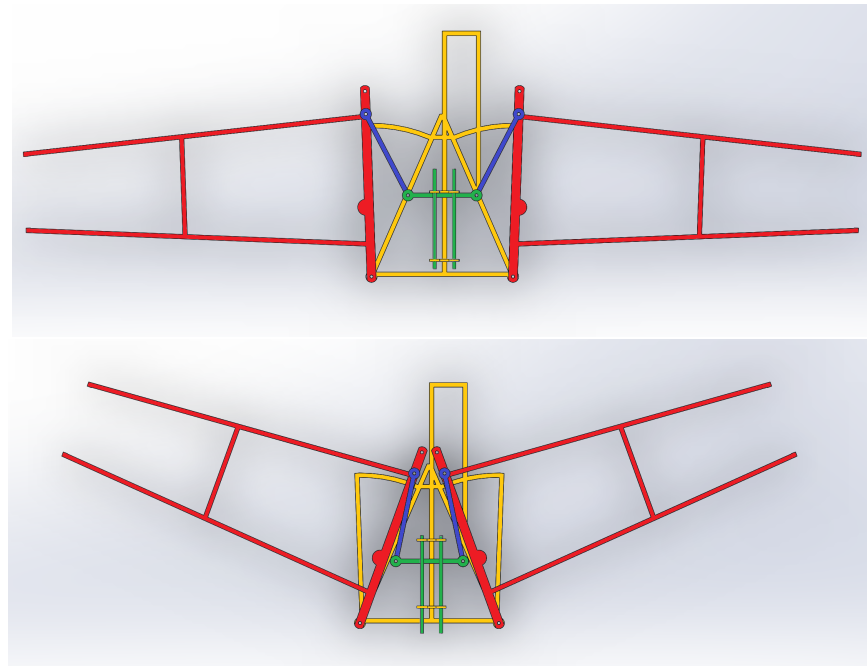

Figure 3. Mechanism in straight (top) and swept (bottom) configurations.

Full-scale models of the straight and 25° forward-swept configurations of our airplane with ailerons deflected at 0° and 20° were built from acrylic of the same thickness as the foam used to construct the actual aircraft. All models were mounted on a 40 centimeter test stand with a revolute joint at their approximate centers of mass. In addition, a servo was connected via a simple two-bar linkage to a second revolute joint aft of the center of mass to adjust the model's pitch while in the wind tunnel. The full test stand assembly is shown in Figure 5.

During preliminary tests, it was found that servo commands sent to the test stand's pitch control mechanism could not be repeatably or precisely correlated with the angle of attack of the model. This was primarily due to backlash in the gears of the servo, and was exacerbated by the varying aerodynamic loads encountered during testing. To ensure accurate measurements of angle of attack, a camera tracking system was used with AprilTags [11] fiducial markers placed on the models. The open-source AprilTags software detects any markers present in a camera image and returns their positions and orientations. A sample image captured during one of our tests and processed by AprilTags is shown in Figure 6. The accuracy of angle measurements made using this system was found to be better than 1°.

To measure aerodynamic forces and moments on the models, the entire test-stand assembly, including the servo and associated electronics, was mounted to a six-axis force and torque sensor (ATI Mini45). Before each test run, two calibration runs were performed: one without a model mounted to the test stand with the wind tunnel fan turned on, and one with the model mounted but the fan turned off. This allowed both the aerodynamic effects of the test stand and
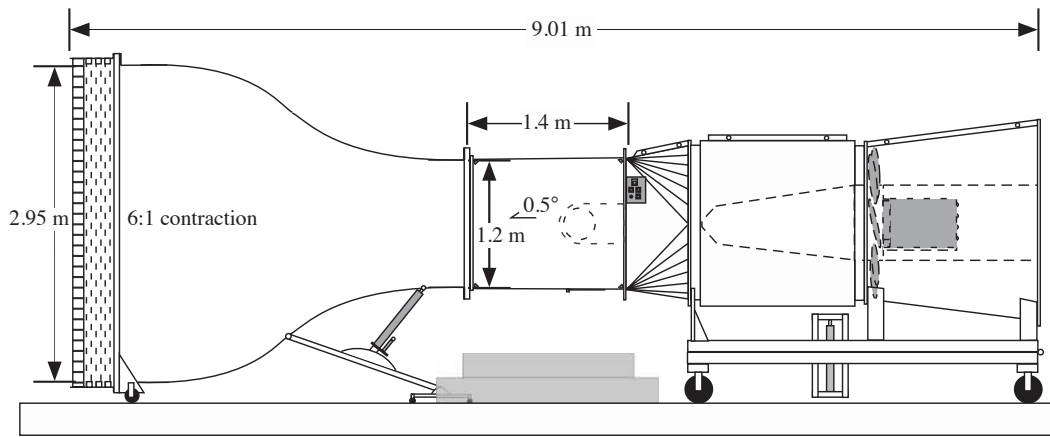
American Institute of Aeronautics and Astronautics

Figure 4. Schematic diagram of the Harvard CFS Wind Tunnel [10].
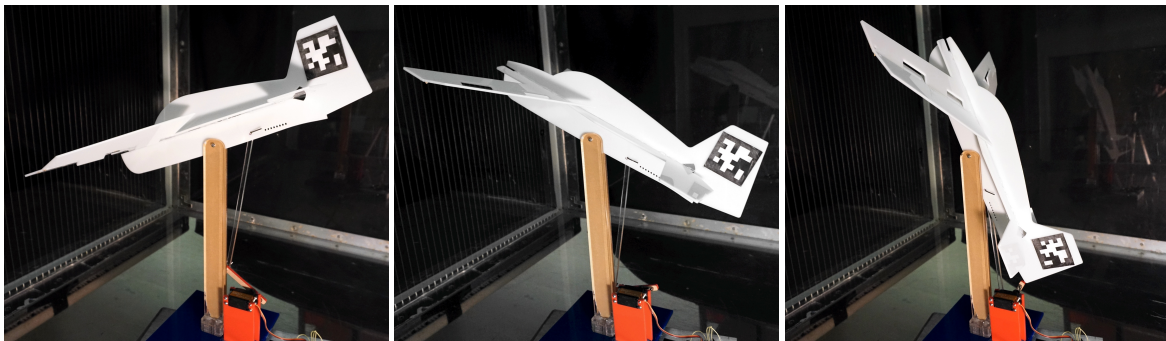

Figure 5. Swept-wing model mounted to test stand at varying angles of attack.
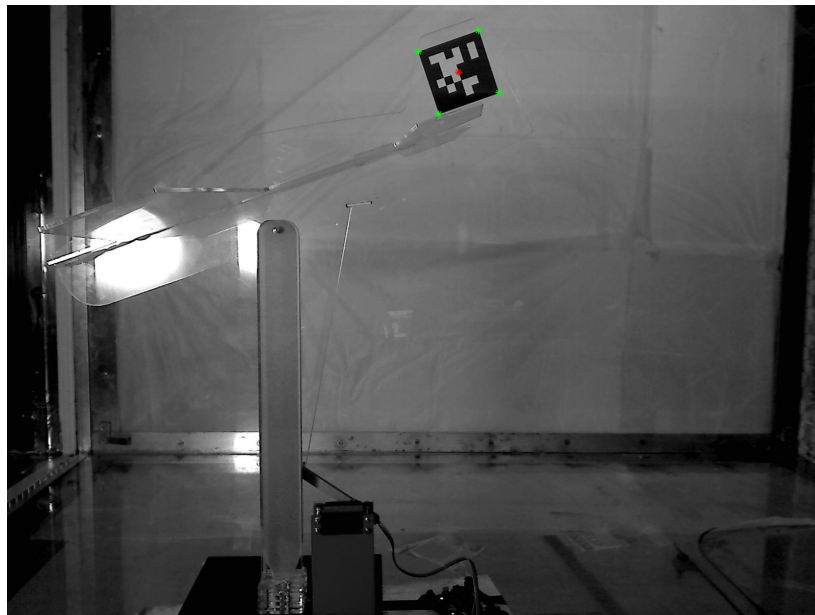

Figure 6. Image from tracking system showing AprilTag detection.

gravitational forces and torques to be subtracted off, leaving only the aerodynamic forces and torques on the model. Real-time data collection was performed with MATLAB. A script capable of communicating with the force and

American Institute of Aeronautics and Astronautics

torque sensor, pitch-control servo, and the camera was written to fully automate test runs. A MATLAB MEX interface was also created for the open-source C implementation of the AprilTags software [11]. During each test, servo commands were sent to sweep the model's angle of attack from −25° to +75° in 50 discrete increments with a wind velocity of 10 meters per second. At each setting, a photo was taken with the camera, then processed with the AprilTags software to recover the angle of attack. One thousand samples were then collected from the force and torque sensor at a 1 kHz sample rate and averaged to produce a single data point before advancing the servo to the next setting.

IV.   Aerodynamic Coefficients

Figure 7 shows raw force data collected during a test run along with an eighth-order polynomial fit to the data by least squares. Due to the slight misalignments between data points collected at the same servo settings during different test
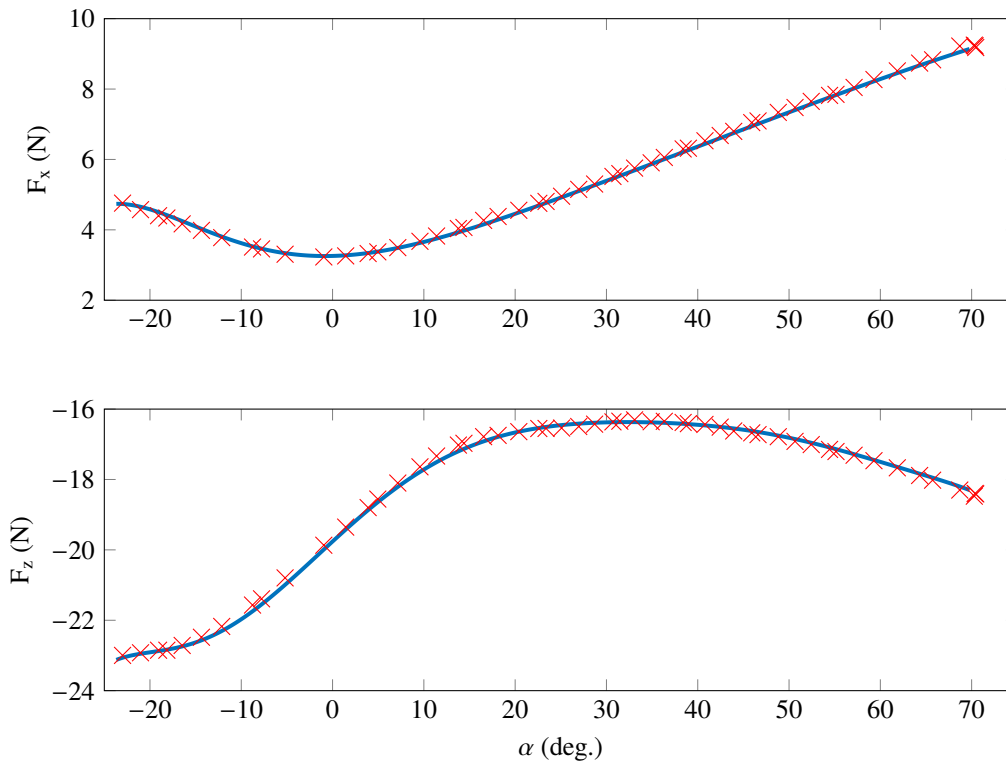

Figure 7. Raw force data with eighth-order polynomial fit.

runs discussed in the previous section, all calculations were performed on polynomials fit to whole data sets rather than individual data points. To eliminate gravitational effects and aerodynamic effects on the test stand, force and torque curves collected with the wind tunnel fan turned off, as well as curves collected without the model mounted to the test stand, were subtracted from the curves shown in Figure 7. Aerodynamic coefficients were then calculated from the standard definitions [12],

$$C_L = \frac{2F_z}{\rho S v^2}, \tag{1}$$

$$C_D = \frac{2F_x}{\rho S v^2}, \tag{2}$$

$$C_M = \frac{2\tau_y}{\rho S c v^2}, \tag{3}$$

where ρ is the air density, S is the planform area of the model, c is the mean chord of the wing, and v is the wind velocity.

Lift and drag coefficients for the straight and forward-swept configurations of the model are plotted in Figure 8. The two wing configurations have nearly identical lift and drag behavior at low angles of attack. However, the forward-swept wing produces more lift (and drag) at high angles of attack. At stall, the forward-swept wing produces roughly 10% greater peak lift, allowing the aircraft to fly slower during perching maneuvers.
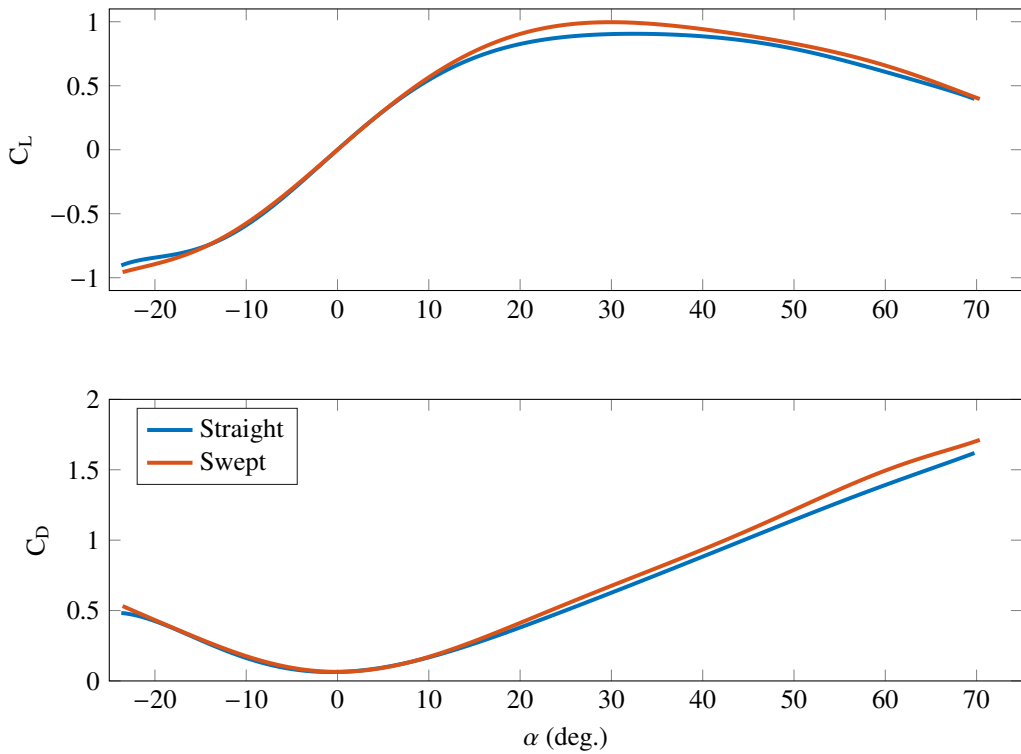
Figure 8. Lift and drag coefficients for straight and swept-wing models.

The moment coefficients for the two wing configurations are plotted in Figure 9. While the straight-wing configuration exhibits uniformly stable pitch behavior, indicated by the negative slope of the C_M curve [13], the forward-swept configuration is very weakly unstable at low angles of attack, and produces much smaller pitching moments at high angles of attack. While undesirable for straight-and-level flight, both of these properties allow the aircraft to be trimmed for flight at high angles of attack with minimal elevator input, avoiding actuator saturation and maintaining greater control authority during perching.
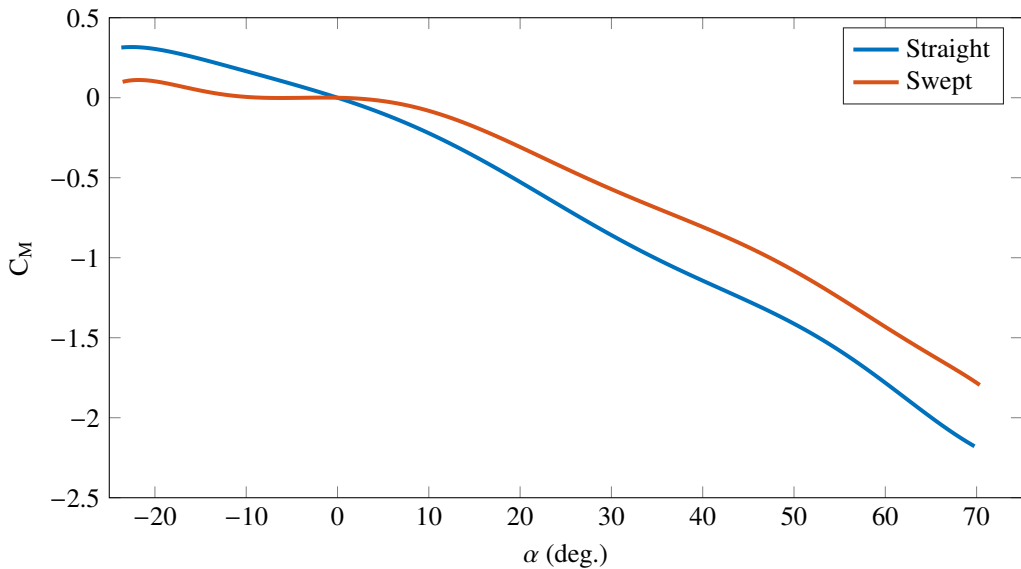

Figure 9. Moment coefficients for straight and swept-wing models.

In addition to the standard aerodynamic coefficients, measurements were also made of the roll moment associated

with a 20° deflection of the ailerons. While it is generally claimed that forward-swept wings maintain better aileron control authority at high angles of attack [7,8], we did not find any evidence for this in our tests. Because the enhanced aileron performance is attributed to delayed wing-tip stall [7], our negative result is likely due to the relatively large size of the ailerons on our model and the fact that they run the full span of the wing.

V. Flight Dynamics Model

Using the aerodynamic coefficient data collected during wind tunnel testing, a nonlinear flight dynamics model that extends to high-angle-of-attack flight regimes has been developed. The model treats the aircraft as a rigid body with mass m and inertia matrix J expressed in the aircraft's body frame. Due to the need to handle high angles of attack, unit quaternions are used to parameterize attitude instead of of Euler angles, which suffer from well-known kinematic singularities [12, 13]. We use the following convention for the components of a unit quaternion [14],

$$q = \begin{bmatrix} \hat{n}\sin(\theta/2) \\ \cos(\theta/2) \end{bmatrix}, \tag{4}$$

where the unit vector $\hat{n} \in \mathbb{R}^3$ represents the axis of rotation and θ is the angle of rotation.

A. Rigid Body Dynamics

The following 13-dimensional vector is used to encode the state of the aircraft,

$$x = \begin{bmatrix} p \\ q \\ v \\ \omega \end{bmatrix}, \tag{5}$$

where $p \in \mathbb{R}^3$ is the position of the aircraft's center of mass in an inertial lab frame, $q \in \mathbb{R}^4$ is the unit quaternion representing the rotation between the aircraft's body frame and the lab frame, $v \in \mathbb{R}^3$ is the aircraft's velocity in the lab frame, and $\omega \in \mathbb{R}^3$ is the aircraft's angular velocity in the body frame. We use the standard aircraft coordinate frame in which $\hat{x}$ points out the nose, $\hat{y}$ points out the right wing tip, and $\hat{z}$ points through the "floor" of the airplane. Control commands are represented by the 4-dimensional input vector,

$$u = \begin{bmatrix} t \\ a \\ e \\ r \end{bmatrix}, \tag{6}$$

where t is the throttle setting, a is the aileron deflection angle, e is the elevator deflection angle, and r is the rudder deflection angle. We assume that actuator dynamics are much faster than the dynamics of the aircraft itself, and thus can be ignored.

The translation dynamics of the aircraft are given by Newton's second law,

$$\dot{v} = \frac{F(x,u)}{m}, \tag{7}$$

where $F(x,u)$ is the total force on the aircraft in the lab frame. Meanwhile, rotation dynamics are given by Euler's equation,

$$\dot{\omega} = J^{-1}\left(\tau(x,u) - \omega^\times J\omega\right), \tag{8}$$

where $\tau(x,u)$ is the total torque on the aircraft in the body frame and $\omega^\times$ is the 3×3 skew-symmetric cross-product matrix:

$$\omega^\times = \begin{bmatrix} 0 & -\omega_3 & \omega_2 \\ \omega_3 & 0 & -\omega_1 \\ -\omega_2 & \omega_1 & 0 \end{bmatrix}. \tag{9}$$

The translation kinematics are simply $\dot{p} = v$, while the rotation kinematics [14] are given by,

$$\dot{q} = \frac{1}{2}M(q)\omega, \tag{10}$$

where $M(q)$ is the following 4×3 matrix:

$$M(q) = \begin{bmatrix} q_{1:3}^{\times} + q_4 I \\ -q_{1:3}^{T} \end{bmatrix} = \begin{bmatrix} q_4 & -q_3 & q_2 \\ q_3 & q_4 & -q_1 \\ -q_2 & q_1 & q_4 \\ -q_1 & -q_2 & -q_3 \end{bmatrix}. \tag{11}$$

B. Forces and Torques

Aerodynamic forces are calculated under the assumption that there is no wind. First, the aircraft's velocity vector is rotated into the body frame and a correction is added to account for prop wash over the aircraft's lifting surfaces,

$$^{\mathcal{B}}v = R(q)^{T} v + \begin{bmatrix} v_{\text{prop}}(t) \\ 0 \\ 0 \end{bmatrix}, \tag{12}$$

where $R(q)$ is the 3×3 rotation matrix formed from the unit quaternion q,

$$R(q) = I + 2q_{1:3}^{\times}(q_{1:3}^{\times} + q_4 I) k, \tag{13}$$

and I is the identity matrix. Prop wash velocity v_{prop} was measured over the full range of throttle settings using a handheld hot wire anemometer and tabulated in a lookup table. From the x and z components of $^{\mathcal{B}}v$, angle of attack is calculated using the two-argument tangent function:

$$\alpha = \text{atan2}(^{\mathcal{B}}v_3, \ ^{\mathcal{B}}v_1). \tag{14}$$

For the rudder, the sideslip angle takes the place of angle of attack, and is defined as,

$$\beta = \text{atan2}(-^{\mathcal{B}}v_2, \ ^{\mathcal{B}}v_1). \tag{15}$$

Lift and drag forces are calculated separately for the left wing, right wing, horizontal tail, and vertical tail, then summed. Control surface deflections are modeled as changes in the effective angle of attack for each lifting surface,

$$\alpha_{\text{eff}} = \alpha + \varepsilon\theta, \tag{16}$$

where θ is the deflection angle (a, e, or r) and ε is the *flap effectiveness* [12], which depends on the ratio of the control surface chord to the total lifting surface chord. We use the polynomial fits to C_L and C_D in Figure 8 for all lifting surfaces. The total lift and drag forces expressed in the body frame are,

$$^{\mathcal{B}}L = \frac{1}{2}\rho v^2 \Big(S_W C_L(\alpha + \varepsilon_a a) + S_W C_L(\alpha - \varepsilon_a a) + S_{HT} C_L(\alpha - \varepsilon_e e) \Big) \begin{bmatrix} \sin(\alpha) \\ 0 \\ -\cos(\alpha) \end{bmatrix}$$
$$+ \frac{1}{2}\rho v^2 S_{VT} C_L(\beta - \varepsilon_r r) \begin{bmatrix} \sin(\beta) \\ \cos(\beta) \\ 0 \end{bmatrix}, \tag{17}$$

$$^{\mathcal{B}}D = \frac{1}{2}\rho v^2 \Big(S_W C_D(\alpha + \varepsilon_a a) + S_W C_D(\alpha - \varepsilon_a a) + S_{HT} C_D(\alpha - \varepsilon_e e) \Big) \begin{bmatrix} -\cos(\alpha) \\ 0 \\ -\sin(\alpha) \end{bmatrix}$$
$$+ \frac{1}{2}\rho v^2 S_{VT} C_D(\beta - \varepsilon_r r) \begin{bmatrix} -\cos(\beta) \\ \sin(\beta) \\ 0 \end{bmatrix}, \tag{18}$$

where S_W, S_{HT}, and S_{VT} are the areas of the wing, horizontal tail, and vertical tail, respectively.

The remaining forces on the aircraft are thrust and gravity. Thrust was measured as a function of throttle setting and found to have a very nearly linear relationship. We therefore express thrust in the body frame as,

$$^{\mathcal{B}}T = t \begin{bmatrix} C_T \\ 0 \\ 0 \end{bmatrix}, \tag{19}$$

American Institute of Aeronautics and Astronautics

where C_T is the constant of proportionality relating throttle setting to force. Summing all terms, the full expression for the force on the aircraft in the inertial frame appearing in equation (7) is:

$$F(x, u) = R(q)\left({}^{\mathcal{B}}L + {}^{\mathcal{B}}D + {}^{\mathcal{B}}T\right) + \begin{bmatrix} 0 \\ 0 \\ -mg \end{bmatrix}. \tag{20}$$

Since gravity and thrust act through the center of mass of the aircraft, only lift and drag contribute to the total torque appearing in equation (8). The moment arm of each lifting surface is the distance d from its center of pressure (assumed to be at the quarter chord) to the center of mass of the aircraft. The torque due to the ailerons expressed in the body frame is:

$$\tau_a = \frac{1}{2}\rho v^2 S_W\left(C_L(\alpha + \varepsilon_a a) - C_L(\alpha - \varepsilon_a a)\right)\begin{bmatrix} d_a \cos(\alpha) \\ 0 \\ d_a \sin(\alpha) \end{bmatrix}$$
$$+ \frac{1}{2}\rho v^2 S_W\left(C_D(\alpha + \varepsilon_a a) - C_D(\alpha - \varepsilon_a a)\right)\begin{bmatrix} d_a \sin(\alpha) \\ 0 \\ -d_a \cos(\alpha) \end{bmatrix}. \tag{21}$$

Similarly, the elevator torque is,

$$\tau_e = -\frac{1}{2}\rho v^2 S_{HT}\left(C_L(\alpha - \varepsilon_e e)\begin{bmatrix} 0 \\ d_e \cos(\alpha) \\ 0 \end{bmatrix} + C_D(\alpha - \varepsilon_e e)\begin{bmatrix} 0 \\ d_e \sin(\alpha) \\ 0 \end{bmatrix}\right), \tag{22}$$

and the rudder torque is,

$$\tau_r = -\frac{1}{2}\rho v^2 S_{VT}\left(C_L(\beta - \varepsilon_r r)\begin{bmatrix} 0 \\ 0 \\ d_r \cos(\beta) \end{bmatrix} + C_D(\beta - \varepsilon_r r)\begin{bmatrix} 0 \\ 0 \\ d_r \sin(\beta) \end{bmatrix}\right). \tag{23}$$

Finally, drag on the propeller blades also produces a torque. This torque was measured and found to have a very nearly linear relationship to the throttle setting:

$$\tau_p = t\begin{bmatrix} -C_\tau \\ 0 \\ 0 \end{bmatrix}. \tag{24}$$

The total torque expressed in the body frame appearing in equation (8) is thus:

$$\tau(x, u) = \tau_a + \tau_e + \tau_r + \tau_p. \tag{25}$$

VI. Perching Trajectories

Using the flight dynamics model developed in the previous section, we now compare the performance of straight and swept wing configurations of our aircraft in simulated perching maneuvers. A direct collocation method based on [15] is used to compute locally optimal perching trajectories. For our purposes, a perch is defined as reaching a specified location with a small residual velocity (a few centimeters per second). We formulate this as a trajectory optimization problem by fixing the aircraft's initial state and constraining its final position to lie within one centimeter of the desired perch. The following cost function, which penalizes final velocity as well as actuator effort, is then minimized,

$$G(x_{1:N}, u_{1:N-1}) = 0.01 \sum_{k=0}^{N-1} u_k^T u_k + 100 \, v_N^T v_N + 10 \, \omega_N^T \omega_N, \tag{26}$$

where subscripts indicate discrete time indices along the sampled trajectory.

Perching trajectories were computed for both straight and forward-swept wing configurations using identical cost functions and initializations, as depicted in Figure 10. First, we note that the forward-swept wing configuration achieved a lower-cost trajectory, with a cost of 311.3 compared to 390.7 for the straight wing. To ensure that this was not simply the result of the straight-wing trajectory becoming trapped in a local optimum, the optimization was repeated with the initial guess for the straight-wing trajectory set to the lower-cost trajectory achieved by the swept-wing airplane. Doing so made no difference in the results.
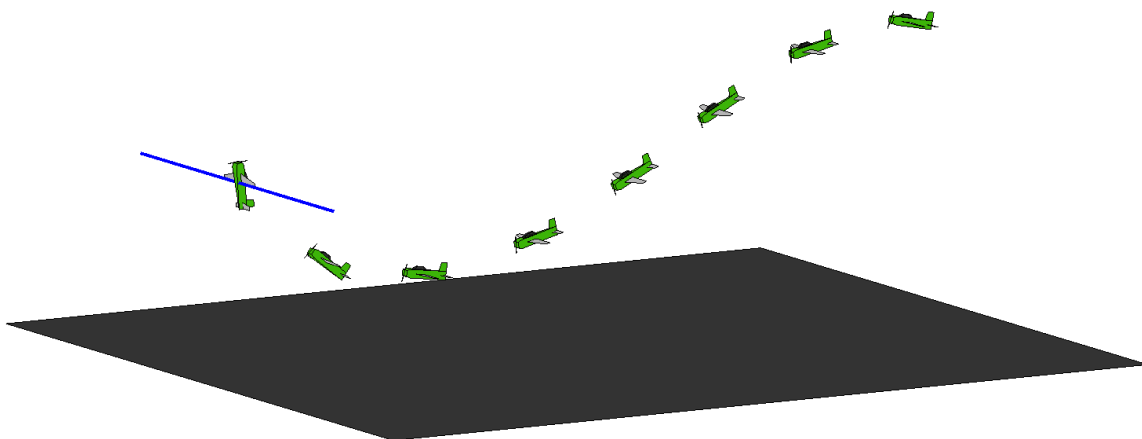
Figure 10. A perching trajectory computed with direct collocation.

Figure 11 plots the angle of attack as a function of time for both aircraft, highlighting a qualitative difference between the two trajectories: The straight-wing airplane performs a "double-flare," raising and lowering its nose once before the final pitch up, while the swept-wing airplane performs only a single flare, pitching the nose up to 90° just before the perch. We believe this effect is attributable to differences in elevator control authority between the two aircraft. Figure 12 plots the throttle and elevator commands for both aircraft during the perching maneuver. Note that
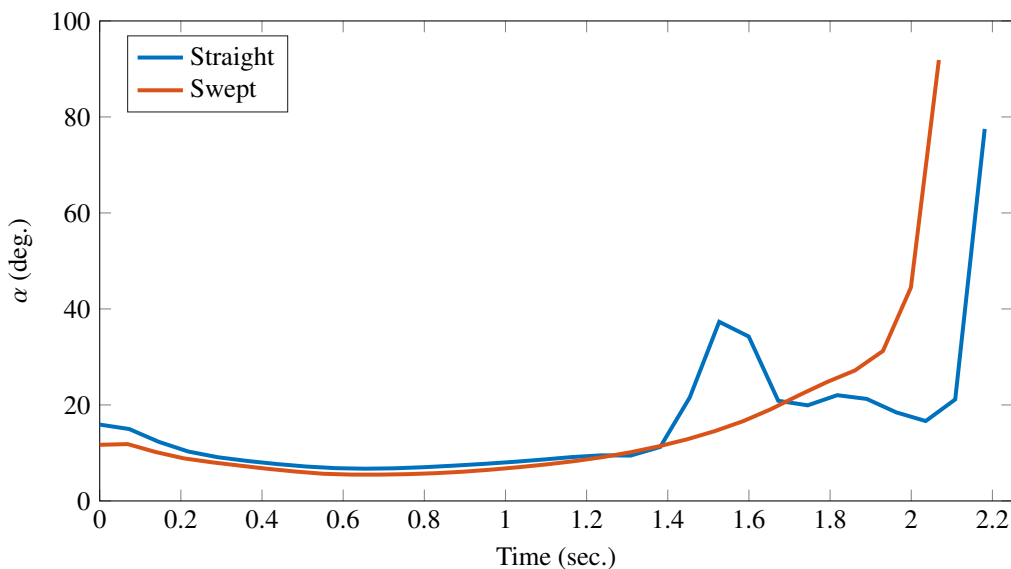

Figure 11. Angle of attack during a perching maneuver.

the elevator saturates at a deflection of approximately −30° during the first flare of the straight-wing airplane, while it remains comfortably within the actuator limits on the swept-wing airplane. The additional flare may be necessary to bleed off sufficient airspeed within the elevator's deflection limits before reaching the perch.

VII. Discussion

The variable-forward-sweep wing concept presented in this paper shows potential for enhancing the agility and performance of micro aerial vehicles. Our wind tunnel testing indicates that sweeping the wings forward increases post-stall lift and can be used to impart a pitching moment or alter the pitch stability characteristics of an aircraft. While we did not observe an improvement in post-stall aileron performance, this was likely due to the particular configuration of the ailerons on our test aircraft. Design modifications and further testing are needed to better understand these effects.

Perching remains an extremely difficult challenge for autonomous aircraft and an area where birds can offer in-
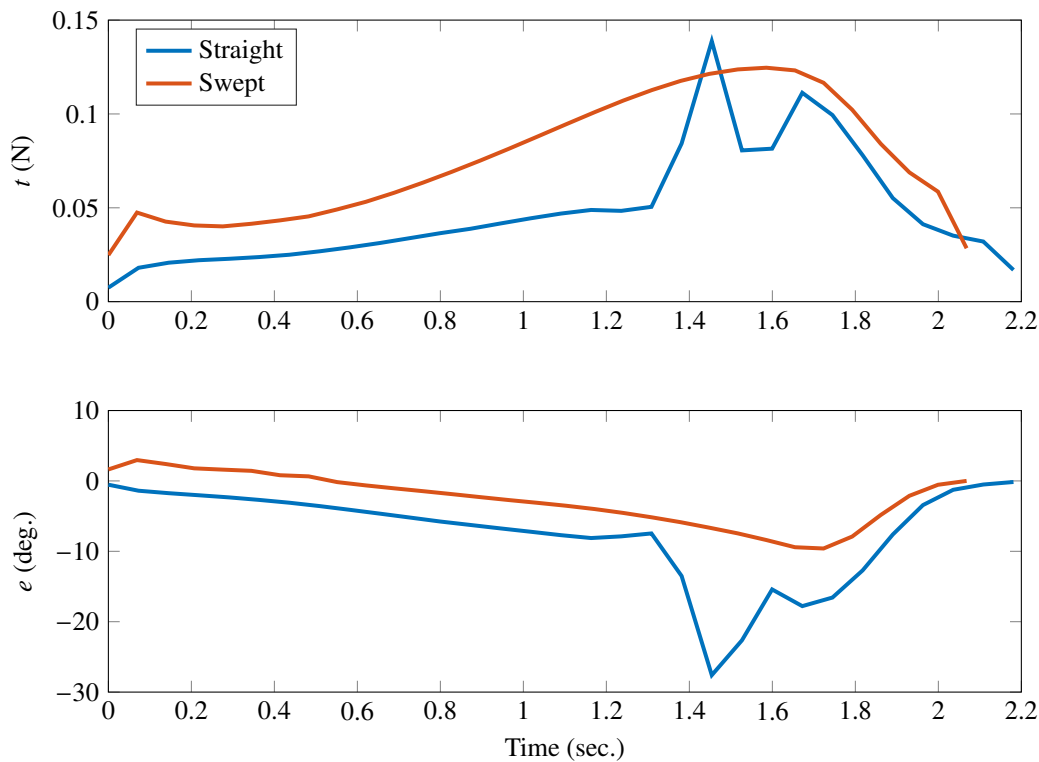
American Institute of Aeronautics and Astronautics

Figure 12. Throttle and elevator commands during a perching maneuver.

spiration and, perhaps, some design guidance. As suggested by avian behavior, our preliminary modeling and control work indicates that a forward-swept wing may provide better performance than a straight wing in such maneuvers. To gain further insight into the dynamics in such extreme flight regimes, our next step will be to reproduce these simulation results with indoor flight experiments.

References

[1] Moore, J., Cory, R., and Tedrake, R., "Robust Post-Stall Perching with a Simple Fixed-Wing Glider Using LQR-Trees," *Bioinspiration & Biomimetics*, Vol. 9, No. 2, June 2014, pp. 025013.

[2] Desbiens, A. L., Asbeck, A. T., and Cutkosky, M. R., "Landing, Perching and Taking off from Vertical Surfaces," *The International Journal of Robotics Research*, Vol. 30, No. 3, Jan. 2011, pp. 355–370.

[3] Wickenheiser, A. M. and Garcia, E., "Optimization of Perching Maneuvers Through Vehicle Morphing," *Journal of Guidance, Control, and Dynamics*, Vol. 31, No. 4, 2008, pp. 815–823.

[4] Wright, K., *Investigating the Use of Wing Sweep for Pitch Control of a Small Unmanned Air Vehicle*, Ph.D. thesis, University of California, San Diego, 2011.

[5] Grant, D., Abdulrahim, M., and Lind, R., "Flight Dynamics of a Morphing Aircraft Utilizing Independent Multiple-Joint Wing Sweep," *AIAA Atmospheric Flight Mechanics Conference and Exhibit*, American Institute of Aeronautics and Astronautics, 2006.

[6] Gomez, J. C. and Garcia, E., "Morphing Unmanned Aerial Vehicles," *Smart Materials and Structures*, Vol. 20, No. 10, 2011, pp. 103001.

[7] Harper, C. and Ralph, M., "A Review of the Stall Characteristics of Swept Wings," Tech. Rep. D-2373, NASA Ames Research Center, 1964.

[8] Putnam, T. W., "X-29 Flight-Research Program," Las Vegas, NV, United States, Jan. 1984.

[9] Thomas, A. L. R. and Taylor, G. K., "Animal Flight Dynamics I. Stability in Gliding Flight," *Journal of Theoretical Biology*, Vol. 212, No. 3, Oct. 2001, pp. 399–424.

[10] Hedrick, T., Tobalske, B., and Biewener, A., "Estimates of Circulation and Gait Change Based on a Three-Dimensional Kinematic Analysis of Flight in Cockatiels (Nymphicus Hollandicus) and Ringed Turtle-Doves (Streptopelia Risoria)," *The Journal of Experimental Biology*, , No. 205, 2002, pp. 1389–1409.

American Institute of Aeronautics and Astronautics

[11] Olson, E., "AprilTag: A Robust and Flexible Visual Fiducial System," *Proceedings of the IEEE International Conference on Robotics and Automation (ICRA)*, May 2011, pp. 3400–3407.

[12] Phillips, W., *Mechanics of Flight*, Wiley, Hoboken, New Jersey, 2nd ed., 2010.

[13] Stengel, R., *Flight Dynamics*, Princeton University Press, Princeton, NJ, 2004.

[14] Schaub, H. and Junkins, J., *Analytical Mechanics of Space Systems*, AIAA Education Series, AIAA, Reston, VA, 2nd ed., 2009.

[15] Hargraves, C. R. and Paris, S. W., "Direct Trajectory Optimization Using Nonlinear Programming and Collocation," *J. Guidance*, Vol. 10, No. 4, 1987, pp. 338–342.